Article

Liquid crystal defect structures with Möbius strip topology

Hanqing Zhao[1], Jung-Shen B. Tai[1], Jin-Sheng Wu [1] & Ivan I. Smalyukh [1,2,3,4] ✉

Topological solitons commonly appear as energy-minimizing field configurations, but examples of stable, spatially localized objects with coexisting solitonic structures and singular defects are rare. Here we use a nonpolar chiral liquid crystal system to show how twist domain walls can co-self-assemble with vortices to form spatially localized topological objects with spontaneous folding. These soliton–vortex assemblies, which we call 'möbiusons', have a topology of the molecular alignment field resembling that of the Möbius strip's surface and package localized field excitations into folded structures within a confinement-frustrated uniform far-field background. Upon supplying energy in the form of electric pulses, möbiusons with different overall symmetries of structure exhibit folding-dependent rotational and translational motions, as well as topological cargo-carrying abilities that can be controlled by tuning the amplitude and frequency of the applied fields. We demonstrate on-demand transformations between various möbiusons and show examples of encoding information by manipulating folds in such structures. A model based on the energetics of solitons and vortices provides insights into the origins of the folding instability, whereas minimization of the Landau–de Gennes free energy closely reproduces details of their internal structure. Our findings may provide a route towards topology-enabled light-steering designs.

Topological solitons and singular defects can enable diverse physical behaviour and technological utility, ranging from dislocation-mediated malleability of metals[1] to Skyrme–Witten descriptions of elementary particles as three-dimensional solitons[2–4] and models of cosmic string emergence after the Big Bang[5]. In liquid crystals (LCs), singular topological defects, which contain spatial regions where molecular ordering directions cannot be defined, typically appear as transient structures[1,2,5–11], although they can be stabilized by colloidal inclusions, patterned boundary conditions and confinement[12–18]. Solitonic structures in chiral LCs can also stabilize singular point and line defects (vortices) against shrinkage or annihilation[2,19,20]. However, the morphology of known field configurations containing such structures is limited to straight-line or looped configurations of twist walls and skyrmions coexisting with singular defects[2]. In this work, we show how solitonic twist walls in a chiral LC can co-self-assemble with vortices and then spontaneously fold into diverse spatially localized configurations. The nonpolar director field $\mathbf{n}(\mathbf{r})$, which describes the average local rod-like LC molecular alignment direction, exhibits highly elaborate, three-dimensional (3D) structures that comprise both solitonic and singular regions with the non-orientable $\mathbf{n}(\mathbf{r})$ tangent to a Möbius strip's surface. These spatially localized excitations, which we call 'möbiusons', spontaneously fold into diverse structures with different symmetries. We reconstruct and numerically model the 3D $\mathbf{n}(\mathbf{r})$ by using nonlinear optical microscopy

[1]Department of Physics, University of Colorado, Boulder, CO, USA. [2]Materials Science and Engineering Program, University of Colorado, Boulder, CO, USA. [3]International Institute for Sustainability with Knotted Chiral Meta Matter, Hiroshima University, Higashihiroshima, Japan. [4]Renewable and Sustainable Energy Institute, National Renewable Energy Laboratory and University of Colorado, Boulder, CO, USA. ✉e-mail: ivan.smalyukh@colorado.edu
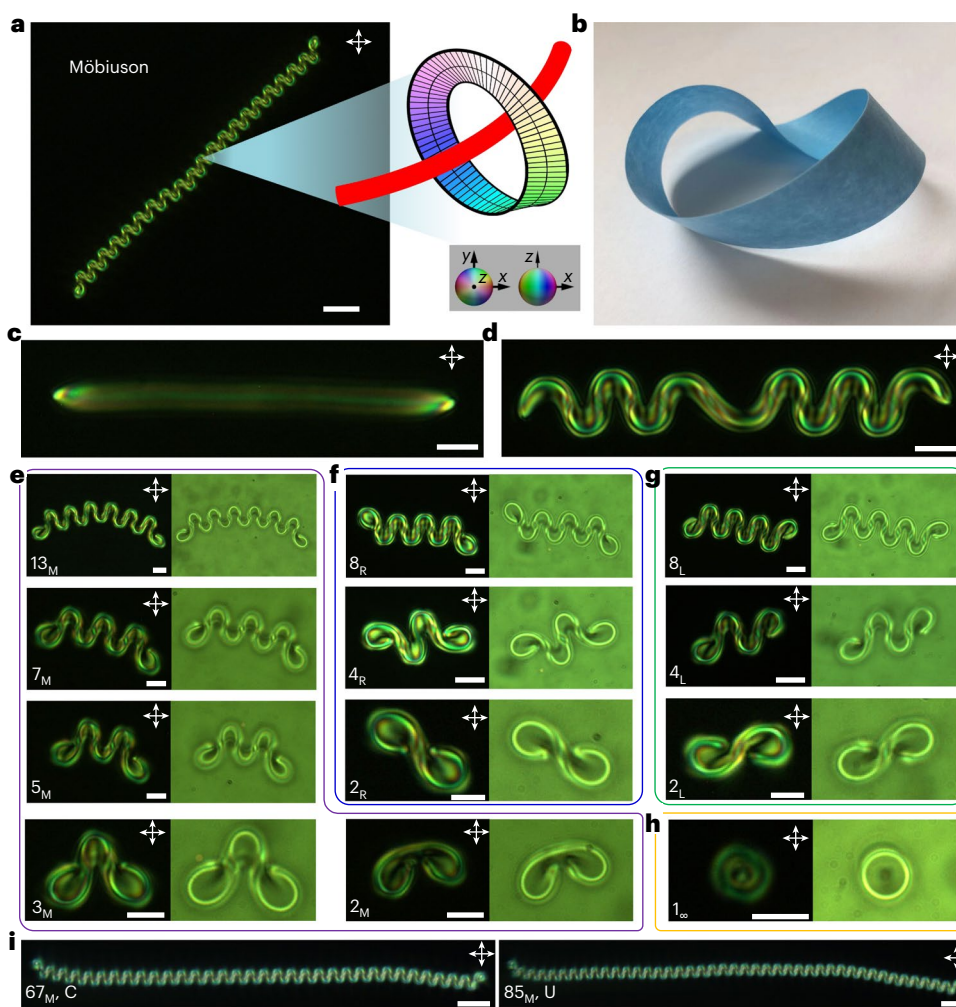
Fig. 1 | The möbiuson family. a, A POM image of an $N = 40$ möbiuson (left, 40_L) and its Möbius-like building blocks (top right), within which the director field is tangent to the surface of a Möbius strip. Here, $\mathbf{n}(\mathbf{r})$ is coloured according to orientations as shown in the colour-coded order parameter space (bottom right). **b**, A Möbius strip made from paper. **c**,**d**, POMs of a linear (**c**) and a spontaneously curved (**d**) fibre-like structure. **e**–**h**, POMs (left) and bright-field images (right) of

möbiusons with mirror symmetry (**e**), right- (**f**) and left-handed folding symmetry (**g**), and D_∞ symmetry (**h**). **i**, Experimental encoding of 'C' and 'U' using the alphabetic ASCII codes, where the number of folds of the möbiuson is correlated to the ASCII table. Cell gap $d = 10\,\mu\text{m}$, pitch $p = 4.6\,\mu\text{m}$ ($d/p = 2.2$) and $U \approx 3.0\,\text{V}$ for all images. The directions of crossed polarizers in POMs are shown by double arrows. Scale bar 30 μm in **a**, 5 μm in **c**–**h** and 30 μm in **i**.

and by minimizing the Landau–de Gennes free energy[1,10–14], respectively, showing how möbiusons emerge from competing free energy contributions. Möbiusons display inter-transformations, symmetry-dependent electrically powered rotational and translational motions and cargo-carrying abilities that exceed the known effects of out-of-equilibrium dynamics of defects and solitons[6–9].

Emergence and inter-transformation of möbiusons

In a glass cell with perpendicular boundary conditions, confinement hinders chiral LC's tendency to twist, causing frustration (Fig. 1a). Möbiusons embed localized fibre-like regions of twisted $\mathbf{n}(\mathbf{r})$, which spontaneously fold and locally relieve the frustration (Fig. 1a). Across these fibre-like regions, $\mathbf{n}(\mathbf{r})$ twists by 180° while being tangent to a Möbius strip (as detailed below), the simplest non-orientable surface with only one side (Fig. 1b). To create a möbiuson, we first apply a voltage of $U \approx 3.5\,\text{V}$ and generate an extended fragment of a localized fibre-like structure with 180°-twisted $\mathbf{n}(\mathbf{r})$ across its width by local melting of the chiral LC using laser tweezers and then quenching

back to the mesophase (Fig. 1c and Supplementary Video 1), a process that allows for embedding topologically nontrivial $\mathbf{n}(\mathbf{r})$ configurations. When a voltage of $U \approx 3\,\text{V}$ is applied across the LC, this fibre-like twisted region spontaneously curves and folds (Fig. 1d and Supplementary Video 1) until eventually relaxing into various stable möbiuson configurations (Fig. 1e–i) that emerge depending on the originally straight fibre's length. These emergent möbiusons are classified based on the number of folds N (Fig. 1e–i) and the symmetry of their polarizing optical micrographs (POMs), where such structures with mirror symmetric and right- or left-handed folding are denoted by N_M, N_R and N_L, respectively. Micrographs of N_M möbiusons contain a single mirror symmetry plane, characterized by the two-dimensional (2D) symmetry group D_1 (Fig. 1e). Each micrograph of N_R or N_L structure contains a two-fold rotation axis (2D symmetry group C_2), whereas N_R and N_L are mirror images of each other (Fig. 1f,g). Even-N möbiusons are either N_R or N_L, with their ends folding counter-clockwise or clockwise, respectively, whereas odd-N möbiusons are N_M. Among special cases (Fig. 1), möbiusons with $N = 2$ exhibit all three types (2_M, 2_R and 2_L), and the ones with $N = 1$ are torons with D_∞ symmetry (Fig. 1h)[2], denoted by 1_∞. Möbiusons can

inter-transform through the creation and annihilation of folds, preserving or changing 2D symmetries. For example, upon increasing the voltage by ~0.02 V beyond the initial equilibrium value, a möbiuson can transform into its lower-N counterpart (Supplementary Video 2). This fold annihilation process reduces N by 2 with the following selection rules: mirror-symmetric möbiusons retain symmetry and transform as $N_M \rightarrow (N-2)_M$, whereas left- or right-handed ones change handedness, that is, $N_R \rightarrow (N-2)_L$ and $N_L \rightarrow (N-2)_R$. However, low-N möbiusons with $N \leq 3$ are exceptions, where $3_M \rightarrow 2_M$ and $N=2$ of all symmetries can transform to 1_∞. These transformations are summarized in Extended Data Fig. 1. To add extra orders of folding to an existing localized excitation, one can grab one end of the initial möbiuson with laser tweezers and stretch it slowly. After turning off the laser, new folds emerge as the elongated möbiuson evolves towards equilibrium (Supplementary Video 3) by following the transformation rules in a reverse order. Stable möbiusons can be used to encode information, as shown in Fig. 1i for the example of 'CU'.

Three-dimensional structures of möbiusons

To understand the mechanism behind the formation of möbiusons, we investigate their internal structures. Before folding, the fibre-like translationally invariant feature (referred to as a cholesteric finger[21,22]; Fig. 1c), comprises a twist wall and two vortex lines (twist disclinations) at the top and bottom substrates, which turn at the finger's ends and close into a single loop (Fig. 2a–c and Extended Data Fig. 2a). This nonsingular wall is a one-dimensional soliton embedded into the background $\mathbf{n}_0$ of the unwound director field, where one-point compactification of its physical space[2,23] connects the equivalent director orientations after the 180° twist, much like in the case of making a Möbius strip from paper (Fig. 1b). A loop of the vortex line embeds the twist wall into the $\mathbf{n}_0$ background, as seen within the cross-sections (Fig. 2a,b), where both the soliton and the vortex are labelled as elements of the first homotopy group, $\pi_1(\mathbb{S}^2/\mathbb{Z}_2)$. The LC order is reduced within the vortex cores and the free energy density is much higher as compared with bulk regions[1,14], whereas the twist wall is energetically favourable due to the LC's intrinsic chirality (Fig. 2a and Extended Data Fig. 2b,c). The electric field applied along $\mathbf{n}_0$ tends to constrain the extent of the twisted region by dielectrically coupling to $\mathbf{n}(\mathbf{r})$. The energy-minimizing shrinking tendency of the vortex line and expanding tendency of the twist wall, both tuneable by applied voltage, thus render the linear configuration of co-assembled soliton and vortex lines unstable, driving them to curve and fold (Figs. 1c–i and 2c–l). Optical micrographs obtained at different depths of focus reveal that the twist wall takes a longer spatial trajectory while the vortex line adopts a shorter one (Fig. 2j and Supplementary Video 4). In high-N möbiusons (Figs. 1i and 2j–l), this leads to multiple folded regions, further lowering the total free energy by optimizing the geometric configurations of walls and singular vortex lines. The formation of möbiusons represents a symmetry-breaking process of the initial linear configuration with D_2 symmetry of the 2D optical image into structures with D_1 or C_2 symmetry. A special case emerges when the initial fibre-like finger fragment is short, so that the two ends interact while curving, eventually merging to yield the 1_∞ toron (Fig. 2c–i and Supplementary Video 5). We reproduce this transformation in numerical simulations using Landau–de Gennes free energy minimization[1,10–14] and confirm that, when the two ends meet, the total free energy is reduced by merging and annihilating the two vertical segments of the high-energy $\pi_1(\mathbb{S}^2/\mathbb{Z}_2) = \mathbb{Z}_2$ vortex line (Fig. 2c–f). The process of merging the finger's ends transforms a single vortex loop into two loops upon reconnection, which then shrink into nanoscale loops identified as $\pi_2(\mathbb{S}^2/\mathbb{Z}_2)$ point defects[2,24]. In the horizontal midplane, the ensuing solitonic structure is the $\pi_2(\mathbb{S}^2/\mathbb{Z}_2)$ skyrmion, which emerges from looping and reconnecting the ends of a $\pi_1(\mathbb{S}^2/\mathbb{Z}_2)$ twist wall (Extended Data Fig. 3). Thus, the overall topological transformation contains reconnection of a single $\pi_1(\mathbb{S}^2/\mathbb{Z}_2)$ twist vortex loop of zero

hedgehog charge into two loops after the finger's ends merge, which then become two $\pi_2(\mathbb{S}^2/\mathbb{Z}_2)$ point defects of opposite relative hedgehog charge (±1), as well as the transformation of a $\pi_1(\mathbb{S}^2/\mathbb{Z}_2)$ twist wall fragment into a $\pi_2(\mathbb{S}^2/\mathbb{Z}_2)$ skyrmion tube terminating at the $\pi_2(\mathbb{S}^2/\mathbb{Z}_2)$ point defects. Remarkably, this transformation between topological objects of different homotopy classes[23] is driven by free energy minimization (Fig. 2f) and involves embedding the solitonic structures into the background $\mathbf{n}_0$ by singular defects of the same homotopy group, both before and after the transformation.

To further probe the 3D structures of möbiusons, we utilize three-photon excitation fluorescence polarizing microscopy (3PEF-PM)[25] synergistically combined with the structural analysis based on minimizing the free energy[10–14]. The 3PEF-PM imaging with different polarizations of the excitation laser light allows for the reconstruction of $\mathbf{n}(\mathbf{r})$, which then serves as initial conditions for the Landau–de Gennes free energy minimization, yielding the equilibrium 3D structures used to simulate 3PEF-PM images (Methods). The agreement between the computer-simulated and experimental images validates the $\mathbf{n}(\mathbf{r})$ reconstruction (Fig. 3, Extended Data Figs. 4 and 5 and Supplementary Video 6), revealing the 3D morphology of the co-assembled vortex lines and twist walls. Around the folds, the twist wall bulges, allowing a larger region of favourable twist while constraining the length of the energetically costly vortex line (Fig. 3i–q and Extended Data Fig. 6), revealing the vortex's shrinking tendency and the twist wall's expanding tendency. The vortex line of 2_M displays mirror symmetry with respect to the vertical plane containing the D_1 mirror plane, but its overall 3D configuration is asymmetric with respect to the cell's horizontal midplane (Fig. 3a–c,g, i–k, Extended Data Fig. 6a and Supplementary Video 6). The vortex loop of 2_R (Fig. 3d–f,h,l–n and Extended Data Fig. 6b) exhibits the two-fold rotation symmetry with respect to the vertical axis along its centre but is also asymmetric with respect to the cell's midplane. The handedness of folding, determined when viewed along the cell substrate's normal, the +z direction, correlates with the vortex loop symmetry, so that the 3D $\mathbf{n}(\mathbf{r})$ of 2_R and 2_L and all the right–left versions of möbiusons can be obtained from one another by flipping the LC sample upside down (Fig. 3 and Extended Data Figs. 7 and 8). Although POM images of 2_R and 2_L distantly resemble twistions[19,20], 3D imaging reveals different topology as these möbiusons comprise $\pi_1(\mathbb{S}^2/\mathbb{Z}_2) = \mathbb{Z}_2$ vortex lines whereas twistions contain $\pi_2(\mathbb{S}^2/\mathbb{Z}_2)$ point defects. The up–down asymmetry of high-N möbiusons manifests itself at the opposite ends of these structures, although they are symmetric with respect to the cell midplane within the central regions comprising many repeated folds (Extended Data Fig. 8b). For möbiusons with many folds, lateral displacement amplitudes of the twist wall D_t and the vortex line D_v from the average centreline and the periodicity of folding L vary with temperature, and the voltage U and the periodicity T_U of the oscillating electric field (Fig. 4). By minimizing the free energy as a function of L, we find that the folded structure has lower free energy than the unwound state or the straight finger, with the equilibrium configuration featuring $L/D_t \approx 1.76$, close to the experimentally measured ratio of $L/D_t \approx 1.84$ (Fig. 4c).

Folding instability within the möbiuson

To gain insights into the möbiuson formation, we constructed an analytical model based on the minimization of the free energy including the vortex lines and the twist wall. The energy density of the vortex line F_v contains contributions from its singular isotropic core (F_c) and elastic deformations of $\mathbf{n}(\mathbf{r})$ around it ($F_v^\mathbf{n}$). F_c can be estimated based on the energy difference between the isotropic and nematic phase and the radius of the isotropic core (r_c). To evaluate $F_v^\mathbf{n}$, we parameterize $\mathbf{n}(\mathbf{r})$ around the top vortex line along y in a möbiuson by using the ansatz (Fig. 4d) $\mathbf{n}_v = \left(0, \cos\left(\frac{1}{2}\tan^{-1}\left(\frac{z}{x}\right) + \frac{\pi}{4}\right), -\sin\left(\frac{1}{2}\tan^{-1}\left(\frac{z}{x}\right) + \frac{\pi}{4}\right)\right)$, where
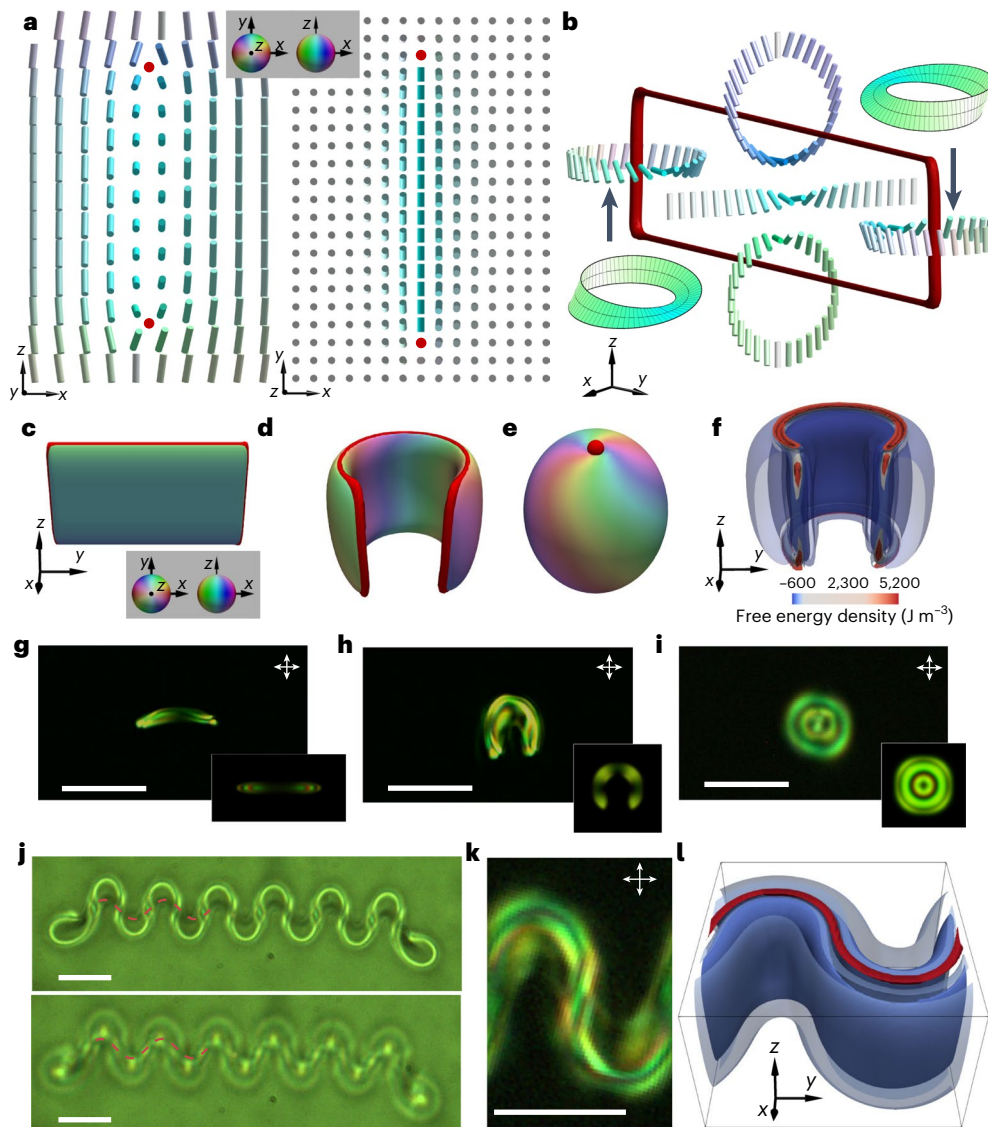
Fig. 2 | Möbiuson formation driven by co-assembly of a vortex line and twist wall. a, $\mathbf{n}(\mathbf{r})$ of a straight extended fibre-like fragment in the mutually orthogonal cross-sections shown by cylinders coloured based on their orientations. **b**, 3D visualization of the straight extended fibre-like fragment as co-assembled vortex line (red) and 180°-twist wall soliton (centre) where the $\mathbf{n}(\mathbf{r})$ around the vortex line form Möbius strips. The singular vortex lines in **a** and **b** are shown in red. **c–e**, Computer-simulated transformation of a straight fibre-like fragment into 1_∞ shown by singular defects (red) and $|n_z| = 0.8$ isosurfaces coloured by $\mathbf{n}(\mathbf{r})$ orientation. **f**, Landau–de Gennes free energy density of a curved fibre-like fragment shown by isosurfaces (dissected for clarity) according to the colour scheme, where the localized high-energy region corresponds to the vortex line.

g–i, POMs of transformation of a straight fibre-like fragment into 1_∞. Computer-simulated POM counterparts are shown in the bottom right insets, where images **g–i** are based on structures shown in **c–e**, respectively. **j**, Optical bright-field images of a 1_{3M} focused at the cell midplane (top) and the vortex line close to one substrate (bottom). The exterior bright feature in the top image shows the spatial extent of the twist wall, and the vortex lines are marked by red dashed lines within the two leftmost repeat periods. **k**, POM of one period of snake-like fragment in a möbiuson. **l**, Free energy density of one period of the snake-like fragment shown by isosurfaces according to the colour scheme in **f**. The free energy density is plotted relative to that of the uniform unwound far-field background. Cell gaps $d = 10\ \mu m$, $d/p = 2.2$ and scale bars indicate 10 μm.

$\mathbf{n}(\mathbf{r})$ twists by 180° along a trajectory around the vortex line while smoothly connecting to the twist wall (Fig. 4d), consistent with the Möbius-strip-like structure. The free energy functional[1]

$$f_{el}[\mathbf{n}] = \frac{K_{11}}{2}(\nabla \cdot \mathbf{n})^2 + \frac{K_{22}}{2}\left[\mathbf{n} \cdot (\nabla \times \mathbf{n}) + \frac{2\pi}{p}\right]^2$$
$$+ \frac{K_{33}}{2}[\mathbf{n} \times (\nabla \times \mathbf{n})]^2 - \frac{\varepsilon_0 \varepsilon_a}{2}(\mathbf{E} \cdot \mathbf{n})^2 \tag{1}$$

contains the first three Frank–Oseen elastic energy terms with elastic constants K_{11}, K_{22} and K_{33} describing the costs of splay, twist and bend deformations, respectively, as well as the dielectric

contribution from the coupling to an external electric field $|\mathbf{E}| = U/d$ along the vertical (z) direction, where ε_a is the LC's dielectric anisotropy and ε_0 is the vacuum permittivity. The ensuing free energy with respect to background per unit length is then derived via integrating equation (1) in the plane perpendicular to the vortex line (Fig. 4d) thus

$$F_v^{\mathbf{n}} = \int_{r_c}^{p/4} r\,dr \int_0^{2\pi} d\theta\, f_{el}[\mathbf{n}_v] = \frac{\pi}{16}\left(4\varepsilon_0\varepsilon_a\,|\mathbf{E}|^2\left(\frac{p^2}{16} - r_c^2\right)\right.$$
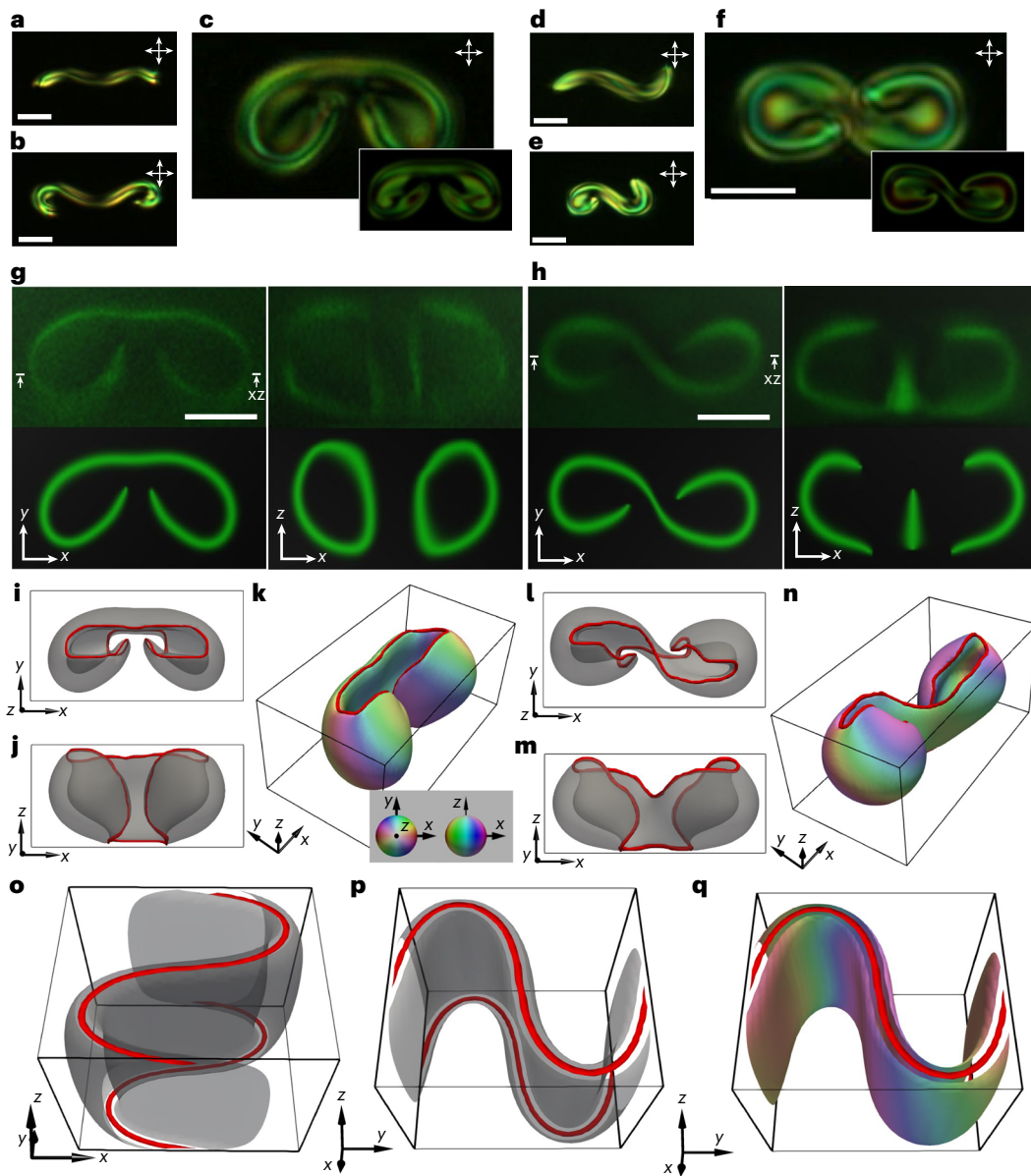$$\left. + (K_{11} + 2K_{22} + K_{33})\ln\left(\frac{p}{4r_c}\right)\right), \tag{2}$$

Fig. 3 | Detailed 3D structures of 2_M and 2_R. a–f, POM snapshots of the formation of 2_M (**a–c**) and 2_R (**d–f**). Computer-simulated counterparts are shown in the bottom right insets in **c** and **f**. **g,h,** Experimental (top) and computer-simulated (bottom) 3PEF-PM images of 2_M (**g**) and 2_R (**h**) obtained with circular polarizations. The positions of the x–z cross-sections are marked in the corresponding x–y cross-sections. Scale bars indicate 5 µm. **i–q,** Computer-simulated structures of 2_M (**i–k**), 2_R (**l–n**) and snake-like fragment in one period (**o–q**) shown by vortex lines (red) and $|n_z| = 0.8$ isosurfaces. In simulations, boundary conditions on the planes orthogonal to the y axis, for which edges are marked by thicker lines, are assumed to be periodic. Isosurfaces in **k**, **n** and **q** are additionally coloured based on $\mathbf{n}(\mathbf{r})$ orientations.

where the radial integral from r_c to $p/4$ is consistent with the observation that $\mathbf{n}(\mathbf{r})$ rotates by $\pi/2$ from the far-field alignment to its centre on either side of the vortex. The shrinking preference of the vortex line is manifested by $F_v > 0$ (Fig. 4e). To calculate the energy for the twist wall, we assume an ansatz of $\mathbf{n}_t = (0, \sin(\frac{\pi x}{w}), \cos(\frac{\pi x}{w}))$ for a wall with a uniform twist rate and width w (Fig. 4d). The associated linear energy density at an applied field reads

$$F_t = \iint d^2\mathbf{r} f_{el}[\mathbf{n}_t] = \frac{whK_{22}}{2}\left(\left(\frac{2\pi}{p} - \frac{\pi}{w}\right)^2 - \left(\frac{2\pi}{p}\right)^2\right) + \frac{wh\varepsilon_0\varepsilon_a|\mathbf{E}|^2}{4},$$

(3)

with h being the height of the twist wall across the sample thickness (along z). Minimizing equation (3) gives the equilibrium width of

an individual twist wall, $w_{eq} = \sqrt{\frac{2\pi^2 K_{22}}{\varepsilon_0\varepsilon_a|\mathbf{E}|^2}}$, which decreases with

increasing $|\mathbf{E}|$, consistent with experiments. The free energy of the twist wall is lower than that of the far-field background, implying an expanding tendency, or spontaneous folding in presence of a length-expanding constraint (Fig. 4e,f). Considering möbiusons observed in experiments and simulations (Figs. 1 and 4c and Supplementary Video 1), we assume that the vortex lines and twist wall follow sinusoidal paths around a common centreline (Fig. 4e and Extended Data Fig. 8a) while having different displacement amplitudes D_v and D_t, respectively, interrelated by an effective width $w = w_{eq} + |D_t - D_v| \sin\left(\frac{2\pi y}{L}\right)$. Such an amplitude difference within a folded structure allows the expansion tendency of the twist wall to be fulfilled while reducing the energy penalty due to
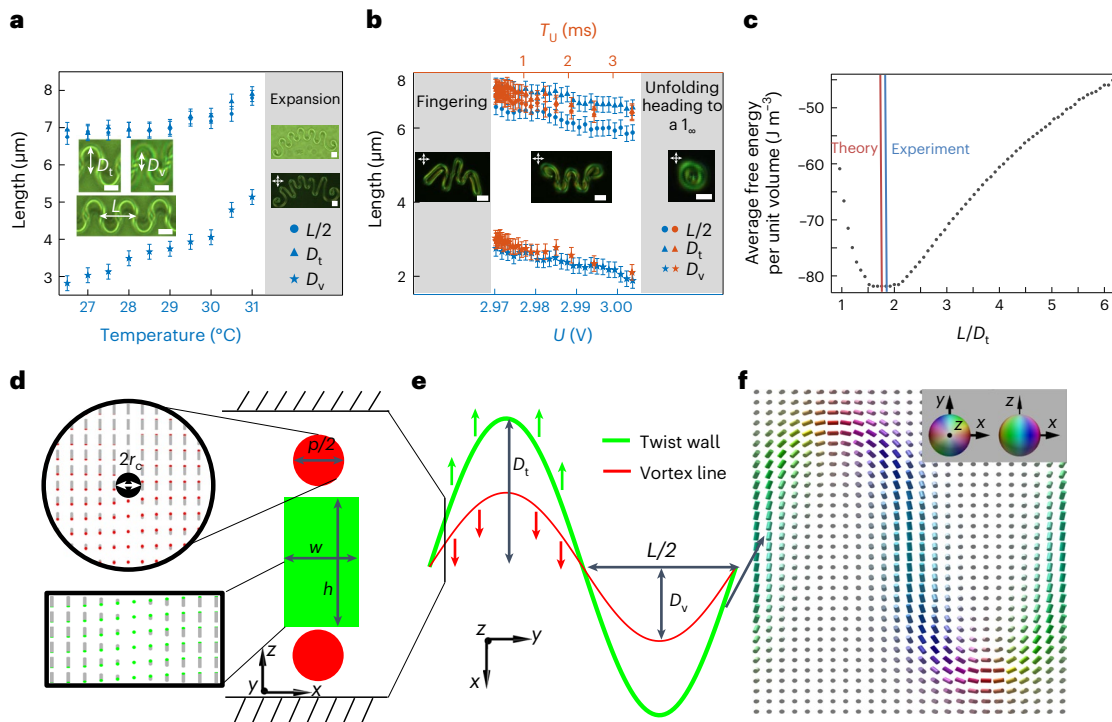
Fig. 4 | Geometric configurations and energetics modelling of möbiusons. a, Temperature dependencies of folding periodicity (L), maximum displacements of twist wall (D_t) and vortex lines (D_v), defined in left insets atop of bright-field images. Right insets show non-equilibrating expansion of the möbiuson when temperature increases above 31.5 °C. **b,** L, D_t and D_v versus the voltage (U) and the periodicity of the oscillating field (T_U). Left inset depicts fingering of a möbiuson observed at $U < 2.970$ V and $T_U < 0.3$ ms. Right inset shows a möbiuson shrunk to a 1_∞ at $U > 3.003$ V and $T_U > 3.3$ ms. Lengths are measured with an error of ±0.2 μm in **a** and **b**, corresponding to the error bars. Scale bars indicate 5 μm. In **b**, red and blue axes and markers correspond to T_U and U, respectively. **c,** Computer-simulated average free energy per unit volume versus L/D_t, with a minimum at $L/D_t \approx 1.76$. The blue and red lines mark the experimental $L/D_t \approx 1.84$ and analytical

$L/D_t \approx 1.75$ results, respectively. The free energy density is calculated relative to that of a uniform background, and the equilibrium L is found analytically for $\varepsilon_a = 13.8$, $K_{11} = 6.4$ pN, $K_{22} = 3.0$ pN, $K_{33} = 10$ pN, $p = 4$ μm, $h = 6.0$ μm, $U = 2.04$ V, $r_c = 10$ nm, $F_c = 12.1$ pN, $D_v = 2.8$ μm and $D_t = 6.4$ μm. **d,** Schematic of twist wall and vortices in a cross-sectional plane of a möbiuson in the analytical model, with the $\mathbf{n(r)}$ of the twist wall and vortex line shown in insets. **e,** A schematic showing displacements of the twist wall and vortex lines from the centre line within a folding period, with shrinking/expanding tendencies depicted by arrows. **f,** Computer-simulated $\mathbf{n(r)}$ in the horizontal midplane of one folding period, shown with cylinders coloured according to their orientations based on the top right inset.

stretching the vortex lines. The total free energy for the volume containing one fold of möbiuson within $0 < y < L$ is then calculated via integrating the linear energy densities along the respective paths of vortex lines and twist wall, $F_{tot} = \int 2F_v \, dl_v + \int F_t \, dl_t$, where

$$dl_i = \sqrt{1 + \left(\frac{2\pi D_i}{L}\cos\left(\frac{2\pi y}{L}\right)\right)^2} \, dy \quad \text{with } i = \text{'v' or 't' indicating the vortex}$$

line or twist wall, respectively. The total free energy of the möbiuson per equilibrium period L reads

$$\frac{F_{tot}}{L} = \frac{2}{L}\int\left(\frac{\pi}{16}\left(4\varepsilon_0\varepsilon_a|\mathbf{E}|^2\left(\frac{p^2}{16} - r_c^2\right) + (K_{11} + 2K_{22} + K_{33})\ln\left(\frac{p}{4r_c}\right)\right) + F_c\right)dl_v$$
$$+ \frac{1}{L}\int\frac{h}{4}\left(2\pi^2 K_{22}\left(\frac{1}{w} - \frac{4}{p}\right) + w\varepsilon_0\varepsilon_a|\mathbf{E}|^2\right)dl_t. \tag{4}$$

The twist wall energy density in a möbiuson decreases with D_t (Extended Data Fig. 9a), whereas that of the vortex lines increases with D_v (Extended Data Fig. 9b). Minimization of equation (4) yields a structure with an equilibrium $L = 11.2$ μm and $L/D_t \approx 1.75$, consistent with experiments (Fig. 4 and Extended Data Fig. 9c). Changes of twist wall displacements with varying $|\mathbf{E}|$ also qualitatively agree with experiments (Extended Data Fig. 9d). Increasing D_t from 0 reduces the overall energy, revealing the folding instability of the linear fibre-like structure ($D_t = 0$) and how möbiusons emerge from the competition between the voltage-dependent shrinking tendency of the vortex line and the expanding tendency of the twist wall (Extended Data Fig. 9).

Self-propulsion of möbiusons and control of topological cargo

When subjected to an oscillating field applied across the cell, along $\mathbf{n_0}$, möbiusons exhibit rotational and translational motions (Fig. 5a–c) dependent on their symmetry. In our LC with positive dielectric anisotropy, the oscillating electric field tends to rotate the möbiuson's $\mathbf{n(r)}$ towards $\mathbf{n_0}$, periodically squeezing it. The balances between the electric, elastic and viscous torques while periodically varying the applied voltage originate nonreciprocal dynamics of $\mathbf{n(r)}$ structures[2,6] and squirming motion of particle-like möbiusons dependent on their symmetry. N_M and $N_{R,L}$ structures exhibit electrically powered translations and rotations, respectively. Meanwhile, 1_∞ torons retain their axial symmetry in an oscillating electric field and display only Brownian motion, differently from LCs with negative dielectric anisotropy, where squirming motions emerge along with field-induced symmetry breaking of $\mathbf{n(r)}$ structures[6–8]. The linear and angular velocities of möbiusons with different symmetries (Fig. 5 and Supplementary Videos 7–9) depend on the frequency f of the applied field. For example, the translational speed of 2_M peaks at 0.4 μm s^{-1} for $f \approx 100$ Hz (Fig. 5a,d and Supplementary Video 7). Above 100 Hz, the speed decays exponentially with f. Above 1,000 Hz, the translational motion of N_M is indistinguishable from Brownian motion (Fig. 5a). At $f \lesssim 100$ Hz, N_M become unstable and shrink following the transformation rules (Fig. 4b and Extended Data Fig. 1). The angular speeds of $N_{R,L}$ rotations depend on f, peaking at low frequencies and decreasing exponentially with f (Fig. 5b). The translational and angular speeds decrease as N increases. The direction
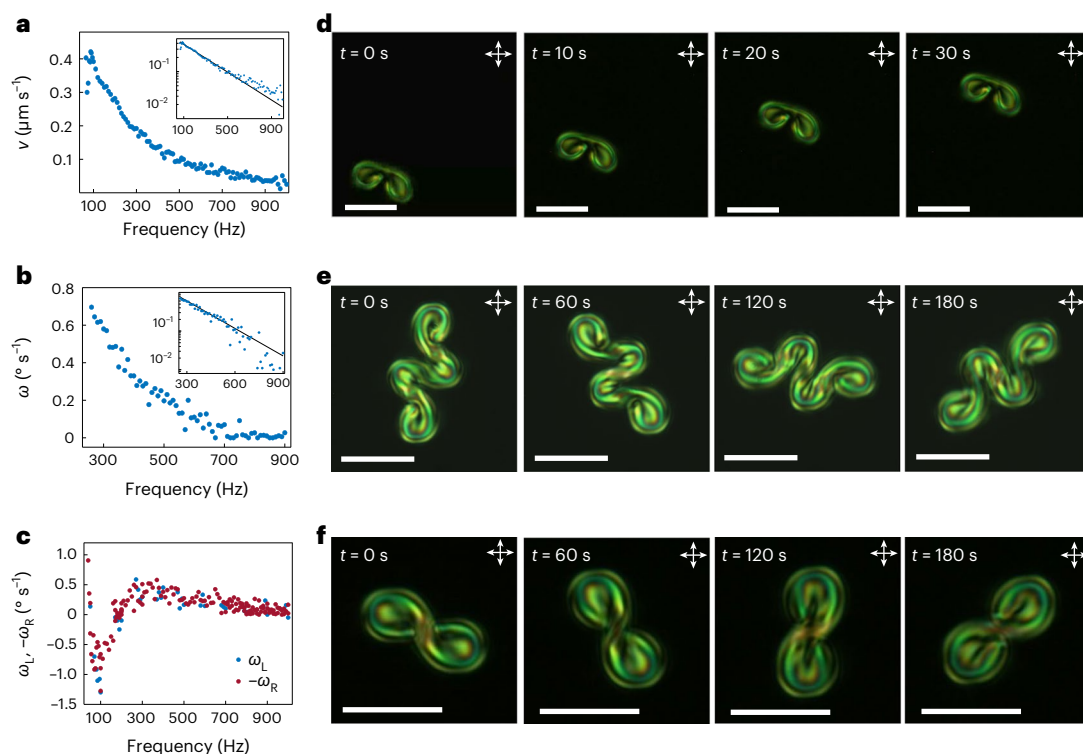
Fig. 5 | Locomotion of möbiusons. a, The translational speed v of 2_M versus the alternating-current (AC) frequency f. Inset: log-scale plot with an exponential fit to the data (black line). **b**, The angular velocity (ω) of 4_L versus f. Inset: log-scale plot with an exponential fit to the data (black line). **c**, ω of 2_L (ω_L, blue) and 2_R (ω_R, red) versus f. The errors in measuring v and ω are $\pm 0.5\,\mu m$ and $\pm 1°$ for 200 s. **d**–**f**, POM snapshots of self-propelling locomotion of a 2_M, 4_L and 2_R, respectively. Scale bars, 10 µm.
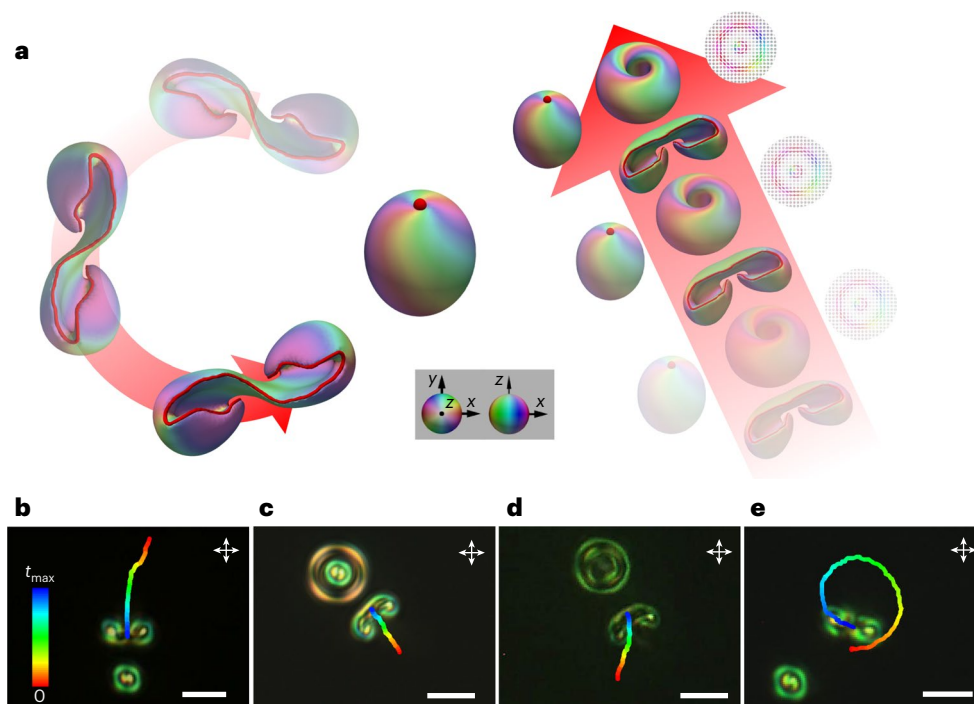
Fig. 6 | Co-propulsion of möbiusons and other solitons. a, Schematic of 'topological dancing' and 'topological cargo transport' of möbiusons. Red arrows show the motion directions. **b**–**d**, Co-propelling motions of 2_M with a toron (**b**), a skyrmion bag (**c**) and a hopfion (**d**). **e**, Topological dancing of 2_R and a toron. Trajectories in **b**–**e** are colour-coded by time according to the scale in **b**, $t_{max} = 120\,s$ for **b**–**d** and 240 s for **e**. Scale bars, 10 µm.

of rotation of 2_R and 2_L reverses as f changes, with the amplitude of the angular speed ω peaking at around 100 Hz ($\omega \approx -1°\,s^{-1}$) and 300 Hz ($\omega \approx 0.4°\,s^{-1}$), where the counter-clockwise direction is defined as

positive (Fig. 5c,f). Examples of the rotational motion of 2_R at different frequencies are shown in Supplementary Video 8. Though rotating in opposite directions, the dependencies of ω on f are generally similar

for 2_R and 2_L and for N_R and N_L (Fig. 5c), consistent with the fact that the left–right versions of möbiusons have similar 3D $\mathbf{n}(\mathbf{r})$ and differ only in terms of their 3D orientations relative to cell substrates (Supplementary Video 9).

Möbiusons can induce dynamics of high-symmetry topological solitons, such as torons, hopfions and skyrmions with axisymmetric $\mathbf{n}(\mathbf{r})$, which by themselves do not exhibit electrically powered motion in LCs with positive dielectric anisotropy. Möbiuson–soliton interactions (Fig. 6a) impart co-propulsions as shown by the solitons' trajectories for 2_M translating a toron (Fig. 6b), a skyrmion bag (Fig. 6c) and a hopfion (Fig. 6d) as topological cargos (Supplementary Video 10). Interesting dynamics emerge from the rotational motion of the 2_R interacting with a toron, which could be called 'topological dancing' (Fig. 6e, Supplementary Video 10). Compared with the self-propelling speed, 0.4 μm s^{-1}, of 2_M at 100 Hz, the speeds of 2_M–soliton complexes for torons, skyrmion bags and hopfions are 0.25, 0.07 and 0.15 μm s^{-1}, respectively, whereas the linear speed along the 'dancing' trajectory in Fig. 5e is 0.26 μm s^{-1}. The different co-propulsion speeds stem from the different effective viscous drag forces of these möbiuson–soliton assemblies, calling for their systematic analysis.

Conclusions and outlook

Möbiusons exhibit diverse folded configurations of co-assembled twist solitons and singular vortices in the order parameter field, both being topological mimics of the Möbius strip. Their non-orientable field configurations cannot emerge in polar systems, such as magnets or ferroelectrics, but potentially could have counterparts in other systems with nonpolar order parameters[1], in polarization fields of light[26] and in other branches of science ranging from particle physics to cosmology[3–5,21]. Electrically powered emergent self-propulsions show möbiuson stability under out-of-equilibrium conditions and might help establish LCs as model systems to explore active matter behaviours and to transport cargo at the mesoscale[27]. While the confinement used in our work partially limits the diversity of folded configurations, even more possibilities could exist without confinement, including vortex–soliton assemblies with knotted configurations and Möbius-strip-like structures on larger scales. Such topology-based designs could enable novel mechanical responses in LC polymers and elastomers[28] and organize nanoparticles into mesoscale spatial patterns[29]. While chirality is known for stabilizing multi-dimensional solitons, we have shown that chirality can stabilize various co-assemblies of topological solitons and vortices, potentially enabling phases of matter analogous to twist grain boundary and blue phases in LCs and the A-phase in magnets[30–37].

Online content

Any methods, additional references, Nature Portfolio reporting summaries, source data, extended data, supplementary information, acknowledgements, peer review information; details of author contributions and competing interests; and statements of data and code availability are available at https://doi.org/10.1038/s41567-022-01851-1.

References

1. Chaikin, P. M. & Lubensky, T. C. *Principles of Condensed Matter Physics* (Cambridge Univ. Press, 1995).
2. Smalyukh, I. I. Review: knots and other new topological effects in liquid crystals and colloids. *Rep. Prog. Phys.* **83**, 106601 (2020).
3. Skyrme, T. H. R. Particle states of a quantized meson field. *Proc. R. Soc. Lond. Ser. A.* **262**, 237–245 (1961).
4. Adkins, G. S., Nappi, C. R. & Witten, E. Static properties of nucleons in the Skyrme model. *Nucl. Phys. B* **228**, 552–566 (1983).
5. Bowick, M. J., Chandar, L., Schiff, E. A. & Srivastava, A. M. The cosmological Kibble mechanism in the laboratory: string formation in liquid crystals. *Science* **263**, 943–945 (1994).
6. Ackerman, P. J., Boyle, T. & Smalyukh, I. I. Squirming motion of baby skyrmions in nematic fluids. *Nat. Commun.* **8**, 673 (2017).
7. Sohn, H. R. O., Liu, C. D. & Smalyukh, I. I. Schools of skyrmions with electrically tunable elastic interactions. *Nat. Commun.* **10**, 4744 (2019).
8. Sohn, H. R. O. & Smalyukh, I. I. Electrically powered motions of toron crystallites in chiral liquid crystals. *Proc. Natl Acad. Sci. USA* **117**, 6437–6445 (2020).
9. Long, C. & Selinger, J. V. Coarse-grained theory for motion of solitons and skyrmions in liquid crystals. *Soft Matter* **17**, 10437–10446 (2021).
10. Ravnik, M. & Žumer, S. Landau–de Gennes modelling of nematic liquid crystal colloids. *Liq. Cryst.* **36**, 1201–1214 (2009).
11. Tkalec, U., Ravnik, M., Čopar, S., Žumer, S. & Muševič, I. Reconfigurable knots and links in chiral nematic colloids. *Science* **333**, 62–65 (2011).
12. Martinez, A. et al. Mutually tangled colloidal knots and induced defect loops in nematic fields. *Nat. Mater.* **13**, 258–263 (2014).
13. Sussman, D. M. & Beller, D. A. Fast, scalable, and interactive software for Landau–de Gennes numerical modeling of nematic topological defects. *Front. Phys.* **7**, 204 (2019).
14. de Gennes, P. G. & Prost, J. *The Physics of Liquid Crystals* 2nd edn (Clarendon, 1993).
15. Hess, A. J., Poy, G., Tai, J.-S. B., Žumer, S. & Smalyukh, I. I. Control of light by topological solitons in soft chiral birefringent media. *Phys. Rev. X* **10**, 031042 (2020).
16. Kos, Ž. & Dunkel, J. Nematic bits and universal logic gates. *Sci. Adv.* **8**, eabp8371 (2022).
17. Poulin, P., Stark, H., Lubensky, T. C. & Weitz, D. A. Novel colloidal interactions in anisotropic fluids. *Science* **275**, 1770–1773 (1997).
18. Smalyukh, I. I. Liquid crystal colloids. *Annu. Rev. Condens. Matter Phys.* **9**, 207–226 (2018).
19. Loussert, C. & Brasselet, E. Multiple chiral topological states in liquid crystals from unstructured light beams. *Appl. Phys. Lett.* **104**, 051911 (2014).
20. Ackerman, P. J. & Smalyukh, I. I. Reversal of helicoidal twist handedness near point defects of confined chiral liquid crystals. *Phys. Rev. E* **93**, 052702 (2016).
21. Tai, J.-S. B. & Smalyukh, I. I. Surface anchoring as a control parameter for stabilizing torons, skyrmions, twisted walls, fingers, and their hybrids in chiral nematics. *Phys. Rev. E* **101**, 042702 (2020).
22. Oswald, P. & Pieranski, P. *Nematic and Cholesteric Liquid Crystals: Concepts and Physical Properties Illustrated by Experiments* (CRC, 2005).
23. Shnir, Y. M. *Topological and Non-topological Solitons in Scalar Field Theories* (Cambridge Univ. Press, 2018).
24. Smalyukh, I. I., Lansac, Y., Clark, N. A. & Trivedi, R. P. Three-dimensional structure and multistable optical switching of triple-twisted particle-like excitations in anisotropic fluids. *Nat. Mater.* **9**, 139–145 (2010).
25. Lee, T., Trivedi, R. P. & Smalyukh, I. I. Multimodal nonlinear optical polarizing microscopy of long-range molecular order in liquid crystals. *Opt. Lett.* **35**, 3447 (2010).
26. Forbes, A., de Oliveira, M. & Dennis, M. R. Structured light. *Nat. Photon.* **15**, 253–262 (2021).
27. Baraban, L. et al. Transport of cargo by catalytic Janus micro-motors. *Soft Matter* **8**, 48–52 (2012).
28. Kragt, A. J., Hoekstra, D. C., Stallinga, S., Broer, D. J. & Schenning, A. P. 3D helix engineering in chiral photonic materials. *Adv. Mater.* **31**, 1903120 (2019).
29. Wang, X., Miller, D. S., Bukusoglu, E., de Pablo, J. J. & Abbott, N. L. Topological defects in liquid crystals as templates for molecular self-assembly. *Nat. Mater.* **15**, 106–112 (2016).
30. Tai, J.-S. B. & Smalyukh, I. I. Static Hopf solitons and knotted emergent fields in solid-state noncentrosymmetric magnetic nanostructures. *Phys. Rev. Lett.* **121**, 187201 (2018).

31. Renn, S. R. & Lubensky, T. C. Abrikosov dislocation lattice in a model of the cholesteric–to–smectic-*A* transition. *Phys. Rev. A* **38**, 2132–2147 (1988).
32. Pišljar, J. et al. Blue phase III: topological fluid of skyrmions. *Phys. Rev. X* **12**, 011003 (2022).
33. Ravnik, M., Alexander, G. P., Yeomans, J. M. & Žumer, S. Three-dimensional colloidal crystals in liquid crystalline blue phases. *Proc. Natl Acad. Sci. USA* **108**, 5188–5192 (2011).
34. Foster, D. et al. Two-dimensional skyrmion bags in liquid crystals and ferromagnets. *Nat. Phys.* **15**, 655–659 (2019).
35. Ackerman, P. J. & Smalyukh, I. I. Diversity of knot solitons in liquid crystals manifested by linking of preimages in torons and hopfions. *Phys. Rev. X* **7**, 011006 (2017).
36. Duzgun, A., Saxena, A. & Selinger, J. V. Alignment induced reconfigurable walls for patterning and assembly of liquid crystal skyrmions. *Phys. Rev. Res.* **3**, L012005 (2021).
37. Zhang, Q., Ackerman, P. J., Liu, Q. & Smalyukh, I. I. Ferromagnetic switching of knotted vector fields in liquid crystal colloids. *Phys. Rev. Lett.* **115**, 097802 (2015).

Methods

Materials and sample preparation

Chiral LCs were prepared by mixing 4-cyano-4′-pentylbiphenyl (5CB; EM Chemicals) or a commercially available nematic mixture E7 (Slichem) with a small amount of a left-handed chiral additive, cholesterol pelargonate (Sigma-Aldrich). To define the equilibrium pitch (p) of the ensuing chiral LCs, the weight fraction of the added chiral dopant was calculated using $C_{dopant} = 1/(h_{htp}p)$, where the helical twisting power $h_{htp} = 6.25~\mu m^{-1}$ for the cholesterol pelargonate additive. Additionally, for high-resolution, aberration-free 3D nonlinear optical imaging, a partially polymerizable chiral LC mixture was prepared by mixing E7-based chiral LC (69%), reactive mesogens RM-82 and RM-257 (at fractions of 12% and 18%, respectively; both from Merck) and ultraviolet-sensitive photoinitiator Irgacure 369 (1%; Sigma-Aldrich). The sample cells were assembled from indium tin oxide (ITO)-coated glass slides or coverslips treated with 25% solution of polyimide SE5661 (Nissan Chemicals) to obtain strong perpendicular (homeotropic) boundary conditions. The polyimide was applied to the substrates by spin-coating at 2,700 rpm for 30 s followed by baking (for 5 min at 90 °C and then for 1 h at 180 °C). The LC cell gap thickness was defined to be 10-15 μm by using silica spheres as spacers between two substrates, and the ratio between the cell gap and the pitch was $d/p = 2.2$. Metal wires were attached to the ITO and connected to an external voltage supply (GFG-8216A; GW Instek) for electric control.

Generating and imaging localized structures in chiral LCs

To generate a möbiuson, we utilized an ytterbium-doped fibre laser (YLR-10-1064, IPG Photonics), operating at 1,064 nm. First, we laser-generated an extended fibre-like fragment in a uniform unwound background under a sinusoidal electric field by using a laser power between 30 and 40 mW (Supplementary Video 1). Then, we switched off the laser and carefully adjusted the voltage to be around 3.0 V such that the fibre-like fragment did not shrink or extend. The two ends of the fibre-like fragment then spontaneously curved, forming möbiusons of various orders and symmetries, depending on the length of the fibre-like fragment and the spontaneous initial curving directions of its ends. High-N structures ($N > 20$) could be generated from a long fibre-like fragment or by adding extra orders to a low-N möbiuson (Supplementary Video 3). Torons, hopfions and skyrmion bags were also generated by laser tweezers by following procedures as reported previously[24,34,35].

Bright-field and polarizing optical microscopy images were obtained by using a multi-modal imaging setup built around an IX-81 Olympus inverted microscope (which is also integrated with the 3PEF-PM imaging setup described below) and charge coupled device cameras (Grasshopper and Flea FMVU-13S2C-CS, Point Grey Research or Spot 14.2 Color Mosaic, Diagnostic Instruments) with 100×, 40× and 20× Olympus objectives with high numerical aperture (NA) of 1.4, 0.75 and 0.4, respectively. The translational speed, angular velocity and trajectories of solitons were analysed by using ImageJ software (National Institutes of Health).

Three-dimensional nonlinear optical imaging

The 3D nonlinear optical imaging of möbiuson structures such as 2_M and 2_R was performed using the 3PEF-PM setup built around the IX-81 Olympus inverted optical microscope integrated with the ytterbium-doped fibre laser[25]. To reduce material birefringence that leads to 3PEF-PM imaging artefacts[35], before imaging, the möbiusons stabilized in the partially polymerizable chiral LC mixture were photo-polymerized by weak ultraviolet illumination and the unpolymerized LC was washed away and replaced by infiltrating an index-matching immersion oil. We used a Ti–sapphire oscillator (Chameleon Ultra II; Coherent) operating at 870 nm with 140 fs pulses at a repetition rate of 80 MHz as the source of the laser excitation light. An oil-immersion 100× objective (NA 1.4) was used to collect the

fluorescence signal. The fluorescence signal was detected by a photo-multiplier tube (H5784-20; Hamamatsu) after a 417/60 nm bandpass filter. The 3PEF-PM imaging involves a third-order nonlinear process[25], during which LC molecules are excited via the three-photon absorption process and the signal intensity scales as $\cos^6\beta$, where β is the angle between the polarization of the excitation light and the long axis (transition dipole) of the LC molecule. Different polarization states of the excitation were controlled by a pair of half-wave and quarter-wave retardation plates. The patterns of strong 3PEF-PM intensity obtained for a linearly polarized excitation beam reveal the spatial regions where $\cos\beta$ is large, reflecting where $\mathbf{n(r)}$ is close to parallel to the polarization of the laser beam (Extended Data Figs. 4 and 5). On the other hand, the laser excitation with circular polarization helps to visualize regions with $\mathbf{n(r)}$ parallel to glass substrates regardless of their azimuthal orientations (Fig. 3g,h). The experimental 3D fluorescence images were processed by applying uniform contrast enhancement and depth-dependent intensity correction and then compared with their numerically simulated counterparts.

Numerical modelling and visualization

We reconstructed the director field configuration of solitons by minimizing the Landau–de Gennes free energy of a continuum representation of a chiral LC, which reads

$$F = \iint f_{surface}\, d^2\mathbf{r} + \iiint f_{bulk}\, d^3\mathbf{r}, \tag{5}$$

where the bulk energy density (f_{bulk}) was integrated over the 3D volume occupied by the LC whereas the surface free energy density ($f_{surface}$) was integrated over the 2D surfaces at the top and bottom interfaces with substrates. The bulk energy density in the Q tensor formalism can be written as[10,11,38]

$$f_{bulk} = \frac{A}{2} Q_{ij}Q_{ji} + \frac{B}{3} Q_{ij}Q_{jk}Q_{ki} + \frac{C}{4}\left(Q_{ij}Q_{ji}\right)^2 + \frac{L_1}{2}\left(\frac{\partial Q_{ij}}{\partial x_k}\right)^2 + \frac{L_2}{2}\frac{\partial Q_{ij}}{\partial x_j}\frac{\partial Q_{ik}}{\partial x_k}$$
$$+ \frac{L_3}{2}\frac{\partial Q_{ij}}{\partial x_k}\frac{\partial Q_{ik}}{\partial x_j} + \frac{L_6}{2}Q_{ij}\frac{\partial Q_{kl}}{\partial x_i}\frac{\partial Q_{kl}}{\partial x_j} + \frac{4\pi}{p}L_4\varepsilon_{ikl}Q_{ij}\frac{\partial Q_{lj}}{\partial x_k} - \frac{1}{2}\varepsilon_0\bar{\varepsilon}E_i^2 - \frac{1}{3}\varepsilon_0\varepsilon_a^{mol}Q_{ij}E_iE_j, \tag{6}$$

where ε_{ikl} is the Levi–Civita symbol, L_i are the elasticity parameters, A, B and C are the nematic material parameters, $\bar{\varepsilon}$ is the average LC permittivity and ε_a^{mol} is the molecular dielectric anisotropy. Summation over all indices is assumed. The molecular tensor order parameter is defined by $Q = \frac{S}{2}(3\mathbf{nn} - I)$ where S is the scalar order parameter and I is the identity matrix. The first three terms in equation (6) correspond to the thermotropic energy that describes the nematic–isotropic transition of the LC, and minimization of the thermotropic energy yields the equilibrium scalar order parameter $S_{eq} = \frac{-B+\sqrt{B^2-24AC}}{6C}$. The next five terms correspond to the elastic energy that comes from the distortion in $\mathbf{n(r)}$, including the terms related to molecular chirality. Together, the thermotropic and elastic terms reflect the energy penalties associated with deviating the molecular director away from its equilibrium configuration and order. The final two terms describe the dielectric coupling between Q and the electric field $\mathbf{E}$. The surface free energy density $f_{surface}$ describing the surface anchoring at the substrates reads

$$f_{surface} = \frac{W}{2}(Q_{ij} - Q_{ij}^{(0)})^2, \tag{7}$$

where W is the anchoring strength and $Q_{ij}^{(0)}$ defines the preferred orientation and order (S_{eq}) of the LC at the surfaces, corresponding to perpendicular boundary conditions in our experiments.

An energy minimization routine based on the variational method was performed to minimize equation (5)[10,11,21]. To reconstruct molecular alignment configurations of möbiusons, $\mathbf{n(r)}$ orientations derived

from 3PEF-PM imaging were used as initial conditions. For all the simulations, the following parameters were used:[10–12] $d/p = 2$, $A = -1.72 \times 10^5 \, \text{J} \, \text{m}^{-3}$, $B = -2.12 \times 10^6 \, \text{J} \, \text{m}^{-3}$, $C = 1.73 \times 10^6 \, \text{J} \, \text{m}^{-3}$, $L_1 = 3.3 \times 10^{-11} \, \text{N}$, $L_2 = 5.3 \times 10^{-11} \, \text{N}$, $L_3 = 0 \, \text{N}$, $L_4 = 9.4 \times 10^{-11} \, \text{N}$, $L_6 = 3.5 \times 10^{-11} \, \text{N}$, $W = 5 \times 10^{-3} \, \text{J} \, \text{m}^{-2}$, which yields $S_{eq} = 0.533$ and the nematic correlation length $\xi = 6.63 \, \text{nm}$. The voltage applied across the cell gap was $U = 7.0 \, \text{V}$. Minimization of möbiusons' free energy was performed on a 3D grid with a spacing of 33.9 nm in all directions, and a typical simulation volume was a cuboid box with $64 \times 112 \times 50$ grid points, corresponding to physical dimensions of $2.17 \times 3.80 \times 1.70 \, \mu\text{m}^3$. Doubling the grid spacing (to 67.8 nm) on a $128 \times 224 \times 100$ grid ($8.6 \times 15.2 \times 6.8 \, \mu\text{m}^3$) did not yield qualitative differences in the minimized field configurations. We note that using grid spacings larger than ξ leads to an underestimation of the free energy of the defect cores. Nevertheless, variations in field configurations at micrometre length scales, which are three orders of magnitude larger than ξ and the size of the defect core, rather than the system's behaviour within the cores of defect lines, are most relevant to our study of möbiuson structure in this work. The excellent agreement between the simulated field configurations and their experimental counterparts justifies the used rescaling and grid spacing, which allowed for modelling of structures containing defects at the expense of nanometre-scale details within their cores. Minimizations of extended fragment structures were performed on a grid with $100 \times 100 \times 100$ points and spacing of 10.17 nm. To gain insights into the origins of the folding instability, we simulated the snake-like fragment of the möbiuson using a computational box with $50 \times L \times 50$ grid points, where L is the length of a repeating unit cell containing the periodically folded structure to be determined by energy minimization. The boundary conditions at the edges of this unit cell on planes orthogonal to the y axis in Fig. 2l are periodic. By minimizing the field configurations with different L values, we obtained the energy-minimizing period L, as well as the equilibrium director configuration and other geometric characteristics of the folded structure. The numerical results agree well with experimental observations.

We simulated POMs by the Jones matrix method using the energy-minimizing $\mathbf{n}(\mathbf{r})$ of solitons[21,38,39]. We first spilt the cell into 50 thin sublayers along the z direction, then the Jones matrix for each pixel in each sublayer was calculated by finding the local optical axis and the ordinary and extraordinary phase retardation. The optical axis is along the local molecular direction, and phase retardation comes from the optical anisotropy of the LC, for example, $n_o = 1.58$ and $n_e = 1.77$ for 5CB. The Jones matrix for the whole LC cell was obtained by multiplying all the Jones matrices for each sublayer. The simulated single-wavelength POM was obtained as the analyser component of the product of the Jones matrix and the incident polarization. Coloured POMs were then obtained as the combination of single-wavelength POMs corresponding to red, green and blue primary colours at wavelengths of 650, 550 and 450 nm, respectively, with intensities matching the light source in the experiment.

The 3D field configurations of solitons were visualized by the isosurfaces of n_z, the vertical component of $\mathbf{n}(\mathbf{r})$, at $|n_z| = 0.8$, coloured according to the orientations of $\mathbf{n}(\mathbf{r})$, as well as by the isosurface of regions of reduced scalar order parameter ($S = 0.45$ for fibre-like fragments and $S = 0.5$ for möbiusons) to visualize singular vortex lines. Computer simulations of the 3PEF-PM images were based on the signal intensity $I_{3PEF–PM} \propto \cos^6\beta$. In both our experiments and simulations, the intensity patterns obtained for different linear polarizations of excitation light were coloured as shown in Extended Data Figs. 4 and 5. Visualizations were performed in ParaView open-source freeware.

Data availability
Source data are provided with this paper. All other data that support the plots within this paper and other findings of this study are available from the corresponding author upon reasonable request.

Code availability
The codes used for the Landau–de Gennes modelling and the simulation of POMs are published in ref. [38]. Other codes used for the numerical calculations are available upon request.

References
38. Mundoor, H., Wu, J.-S., Wensink, H. H. & Smalyukh, I. I. Thermally reconfigurable monoclinic nematic colloidal fluids. *Nature* **590**, 268–274 (2021).

39. Yeh, P. & Gu, C. *Optics of Liquid Crystal Displays* (Wiley, 1999).

Author contributions
H.Z. and J.-S.B.T. performed experiments and H.Z. and J.-S.W. performed numerical and analytical modelling, under the supervision of I.I.S. I.I.S. conceived and directed the research. H.Z., J.-S.B.T., J.-S.W. and I.I.S. wrote the manuscript.

Competing interests
The authors have no competing interests.

Additional information
Extended data is available for this paper at https://doi.org/10.1038/s41567-022-01851-1.

Supplementary information The online version contains supplementary material available at https://doi.org/10.1038/s41567-022-01851-1.

Correspondence and requests for materials should be addressed to Ivan I. Smalyukh.

Peer review information *Nature Physics* thanks the anonymous reviewers for their contribution to the peer review of this work.

Reprints and permissions information is available at www.nature.com/reprints.
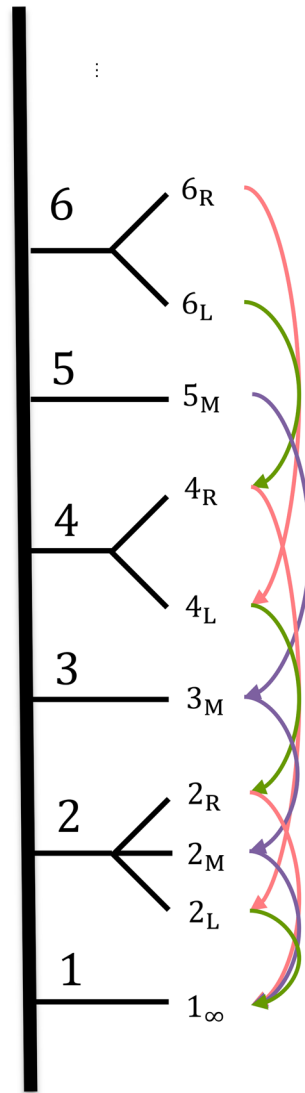
Extended Data Fig. 1 | Selection rules for the inter-transformations of möbiusons. The coloured arrows show transformation cascades starting from a möbiuson with right-handed folding symmetry (red), left-handed folding symmetry (green) or mirror symmetry (purple).
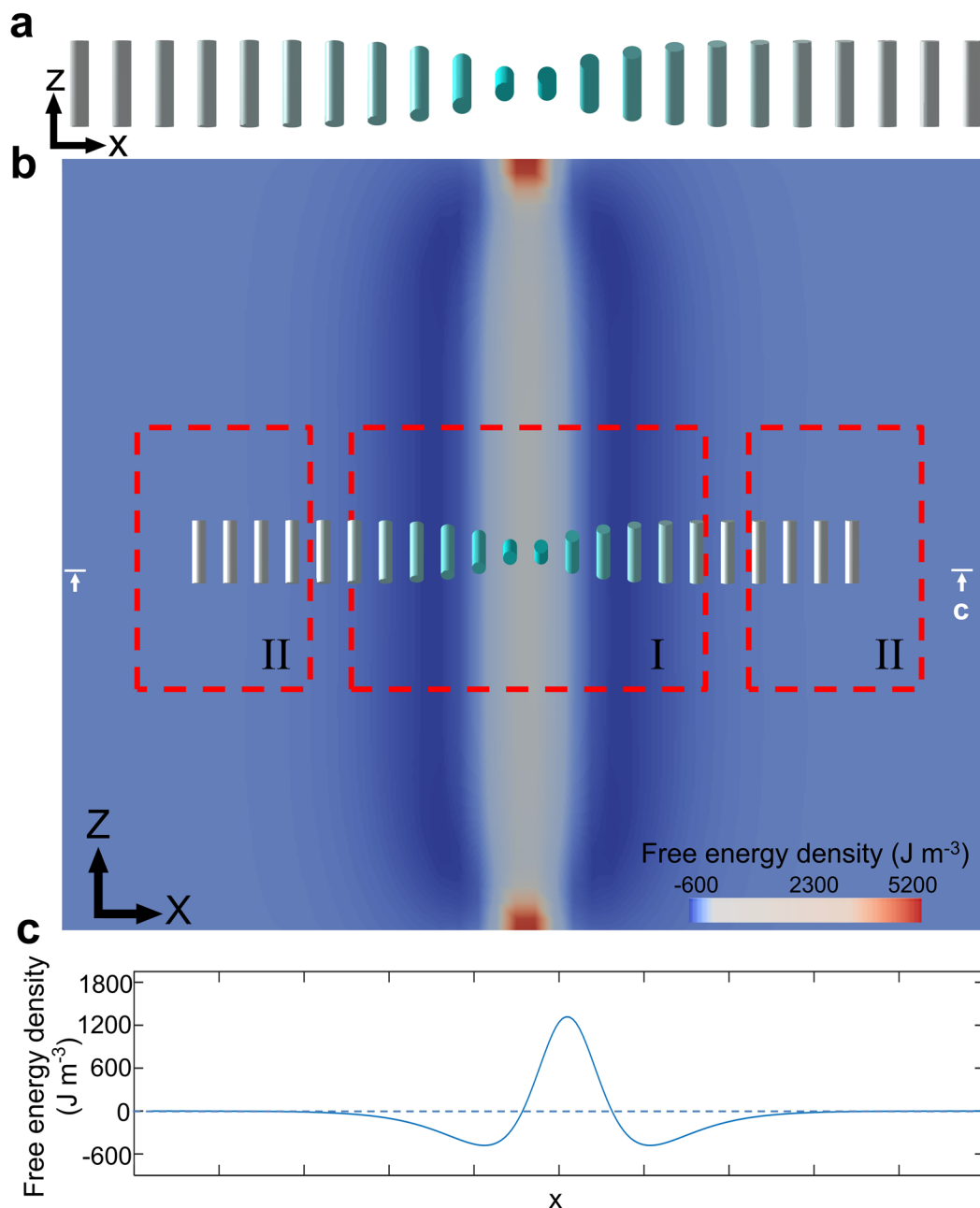
Extended Data Fig. 2 | Twist wall and near-surface twist disclinations of a fibre-like fragment. a, Schematic of a twist wall. The non-polar director field with head-tail symmetry is shown by cylinders that twist by 180°, matching the uniform unwound far-field background $\mathbf{n}_0$ along the z direction. **b**, Free energy density of an extended fibre-like fragment stabilized at an applied electric field in the cross-sectional plane perpendicular to the direction of translational invariance. The average free-energy density of the twisted region (region I) is lower than that of the unwound far-field background (region II) and is plotted relative to the far-field background. The increased values of free energy density in the middle of the twist wall is higher due to the contribution of the dielectric coupling term. **c**, Free energy density along x coordinate in the z-midplane marked in (**b**). The blue dashed line corresponds to the free energy density of the far-field background.
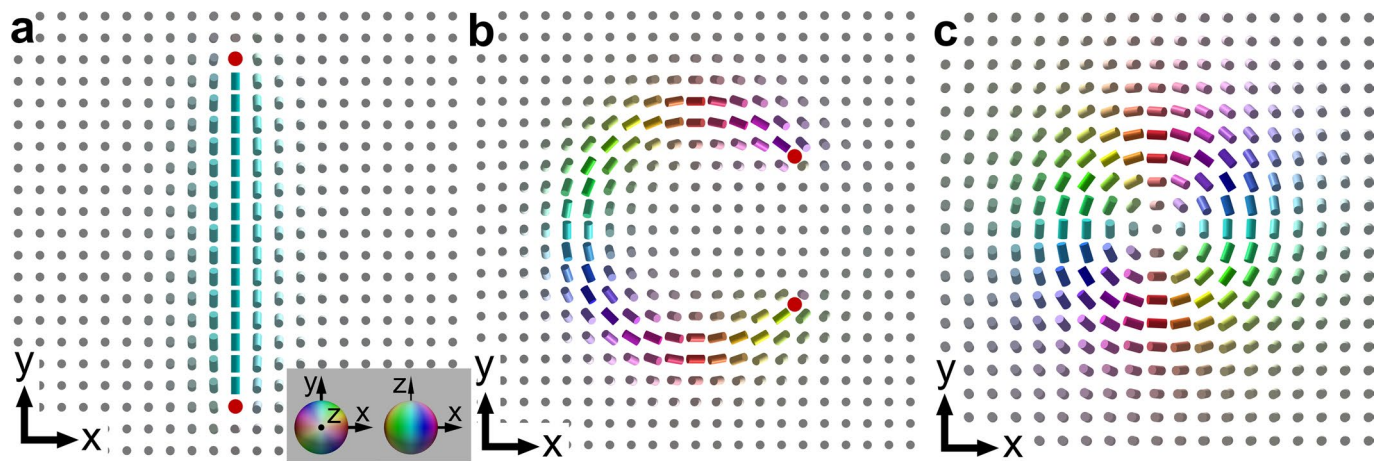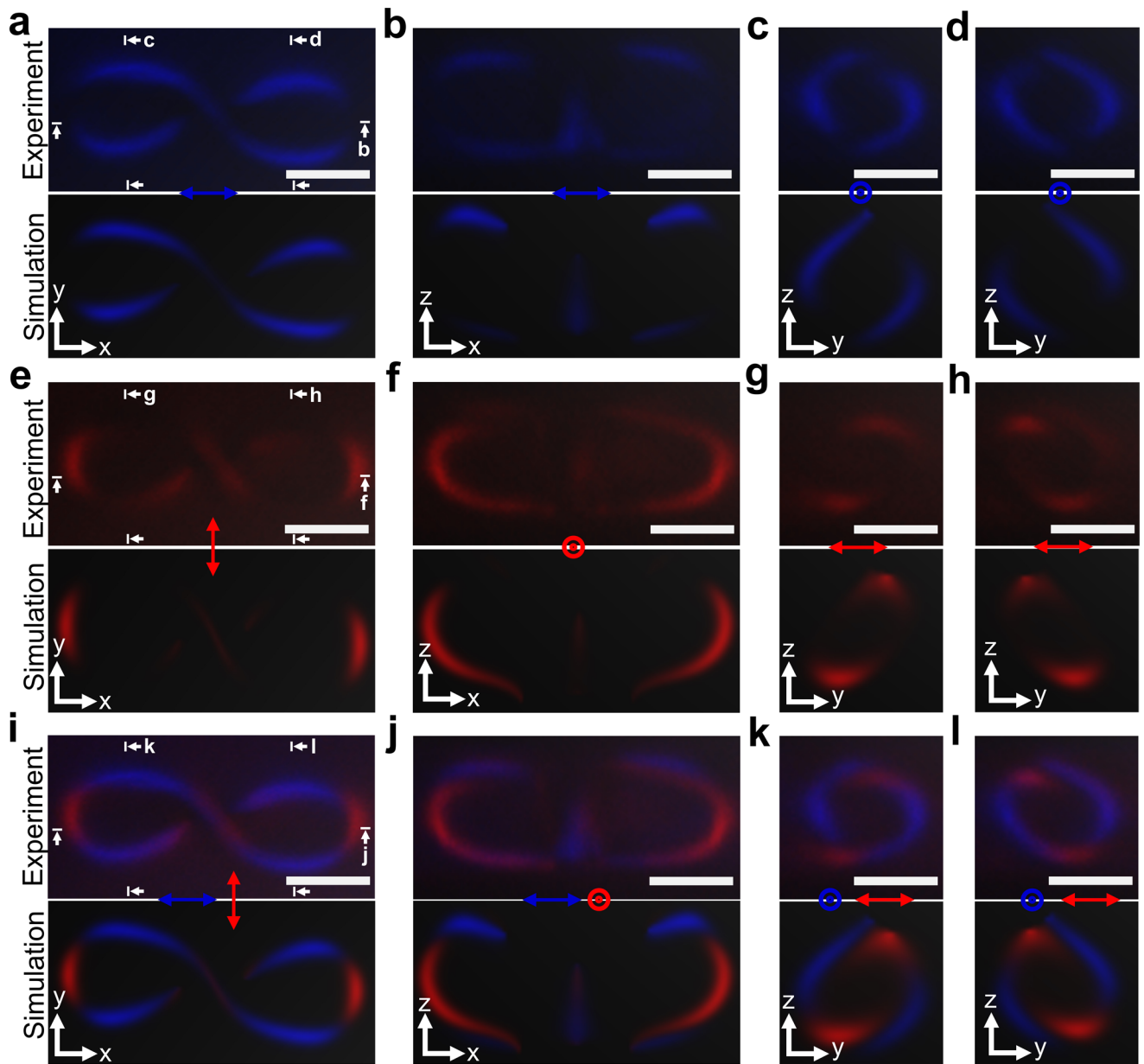
Extended Data Fig. 3 | Computer-simulated formation of 1_∞ from a fibre-like fragment. a-c, Computer simulated cross-sections in the horizontal midplane of a straight fibre-like fragment (**a**), a curved fibre-like fragment (**b**) and a 1_∞ (**c**). The intersections of singular vortex lines in the sample midplanes shown in (**a**) and (**b**) are depicted with the red filled circles. The director field is shown with cylinders coloured according to director orientations based on the bottom-right inset in (**a**).
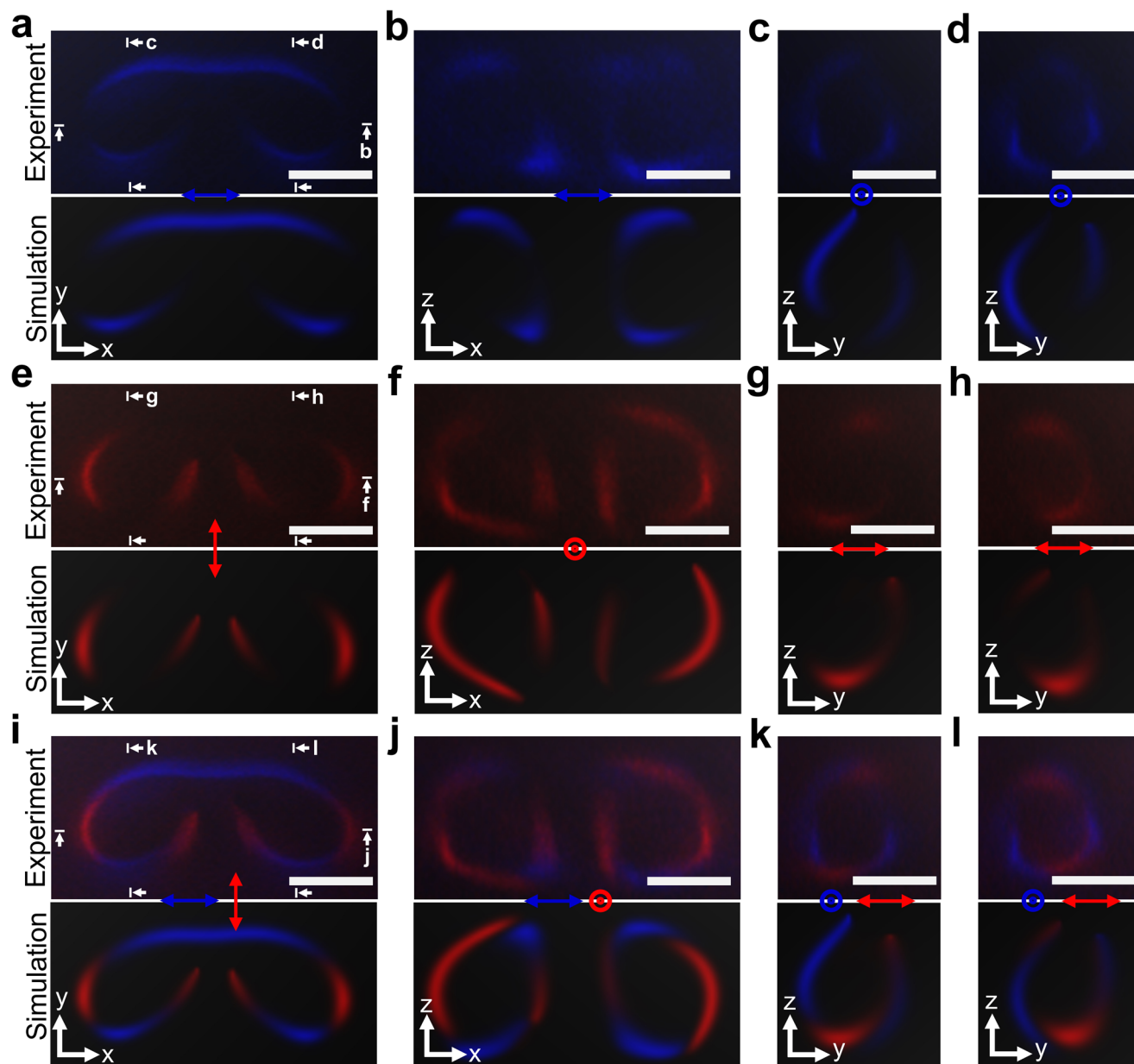
Extended Data Fig. 4 | 3PEF-PM images of 2$_M$. a-h, Experimental (top) and computer-simulated (bottom) 3PEF-PM images of $\mathbf{n}(\mathbf{r})$ in various cross-sections of a 2$_M$ obtained with different polarizations of excitation light. The linear polarizations of excitation light are marked with blue (**a-d**) and red (**e-h**) arrows, respectively. **i-l**, Superposition of 3PEF-PM images obtained with orthogonal linear polarizations of excitation light from (**a-d**) and (**e-h**). The viewing cross-sections are marked in (**a,e** and **i**) correspondingly. Scale bars indicate 5 μm.

Extended Data Fig. 5 | 3PEF-PM images of 2_R. a-h, Experimental (top) and computer-simulated (bottom) 3PEF-PM images of $\mathbf{n}(\mathbf{r})$ in various cross-sections of a 2_R obtained with different polarizations of excitation light. The linear polarizations are mutually orthogonal and marked with blue (**a-d**) and red (**e-h**) arrows, respectively. **i-l**, Superposition of 3PEF-PM images with orthogonal linear polarizations of excitation from (**a-d**) and (**e-h**). The viewing cross-sections are marked in (**a,e** and **i**), correspondingly. Scale bars indicate 5 μm.
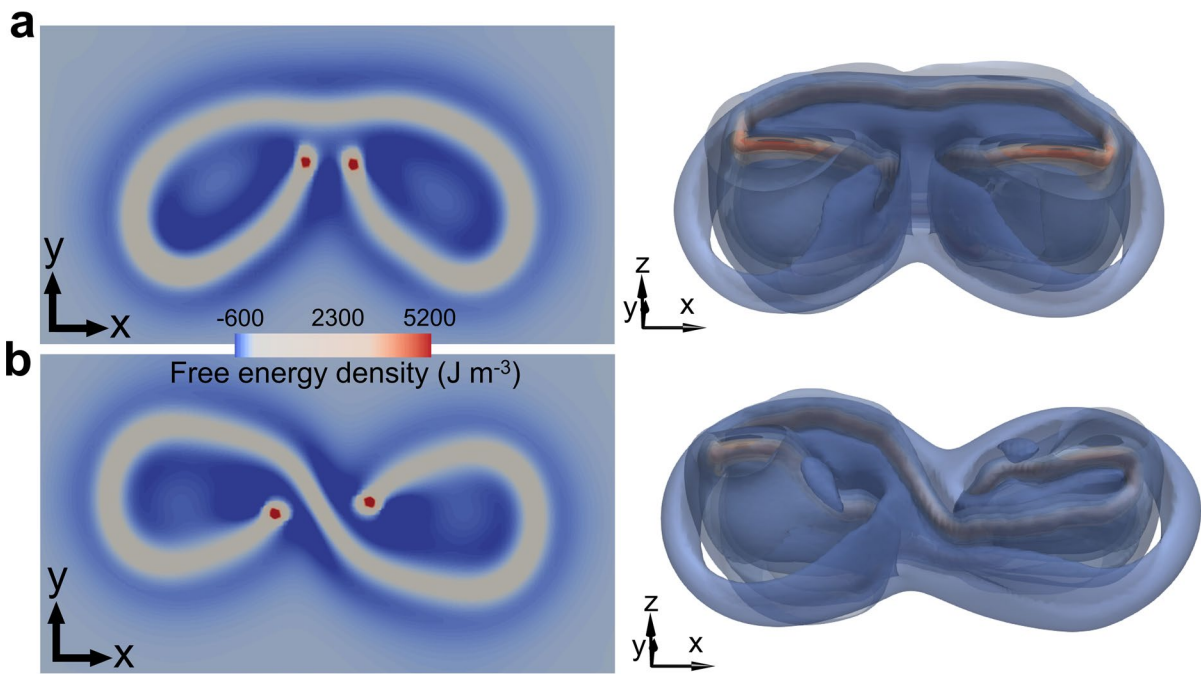
Extended Data Fig. 6 | Free energy density of 2_M and 2_R. a,b, The horizontal midplane cross-section (left) and 3D isosurfaces (dissected for clarity) of free energy density (right) of 2_M (**a**) and 2_R (**b**). The free energy density is plotted relative to that of the uniform unwound far-field background.
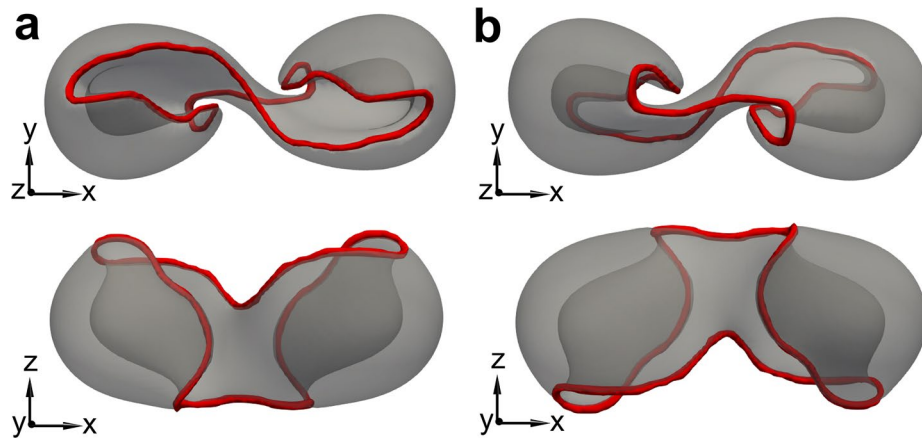
Extended Data Fig. 7 | Visualizations of 2_R and 2_L with loops of similar vortices in 3D. a,b, Field configurations of 2_R (**a**) and 2_L (**b**) visualized by using $|n_z| = 0.8$ isosurfaces (grey) and reduced scalar-order parameter $S = 0.5$ regions for vortex lines (red). By flipping the LC sample by 180°, the configurations of 2_R (**a**) and 2_L (**b**) can be obtained from one another.
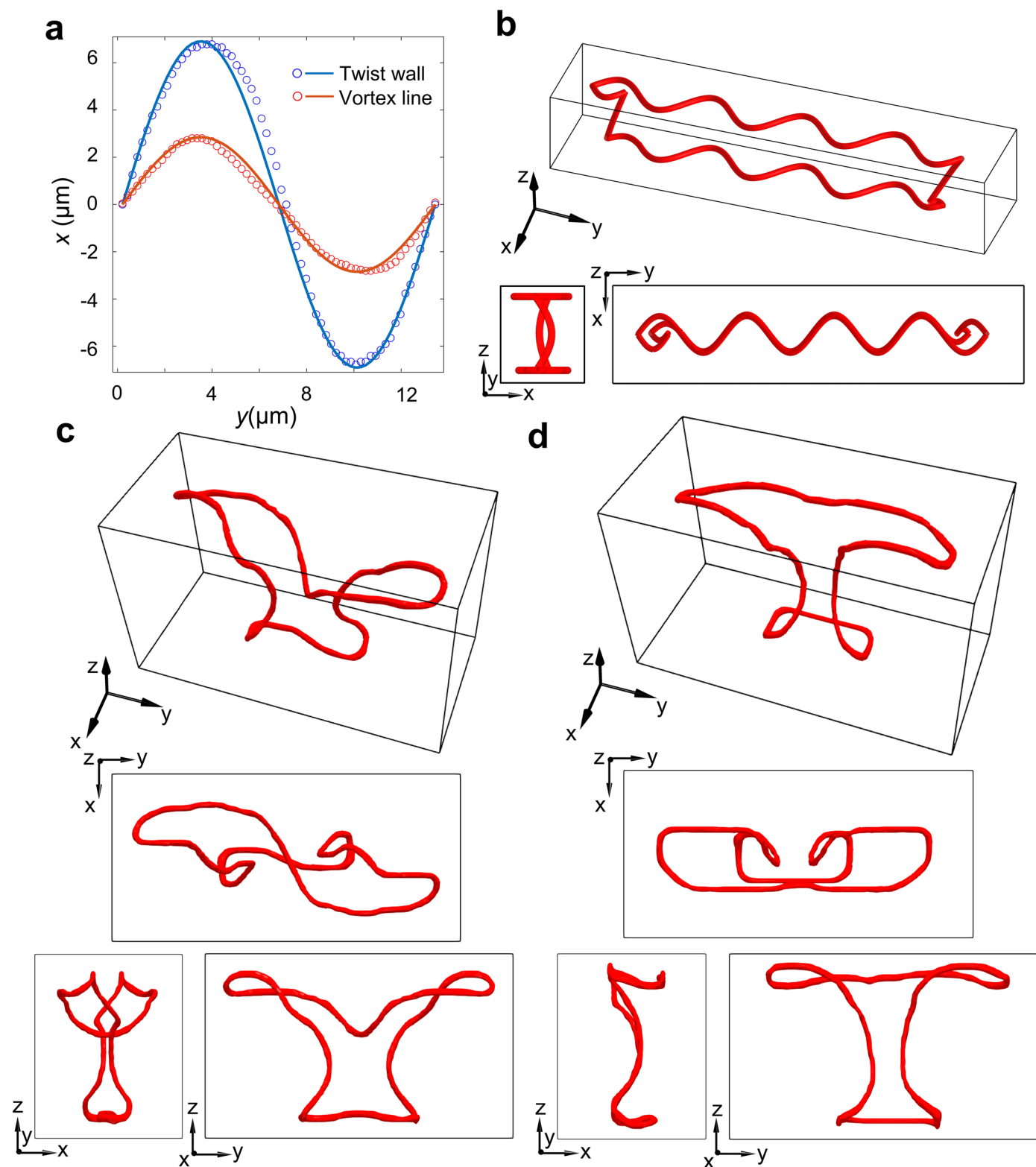
Extended Data Fig. 8 | Spatial configurations of the twist wall and vortex line. a, Displacements of twist wall and vortex lines in xy plane. The blue and red circles correspond to displacements of twist wall and vortex line from the centreline extracted from 2D images. The blue and red solid lines represent the corresponding fitted sinusoidal functions. **b**, 3D trajectory of the vortex line in a high-N möbiuson. **c,d** 3D visualization of the vortex lines extracted from the simulation of a 2_R (**c**) and 2_M (**d**).
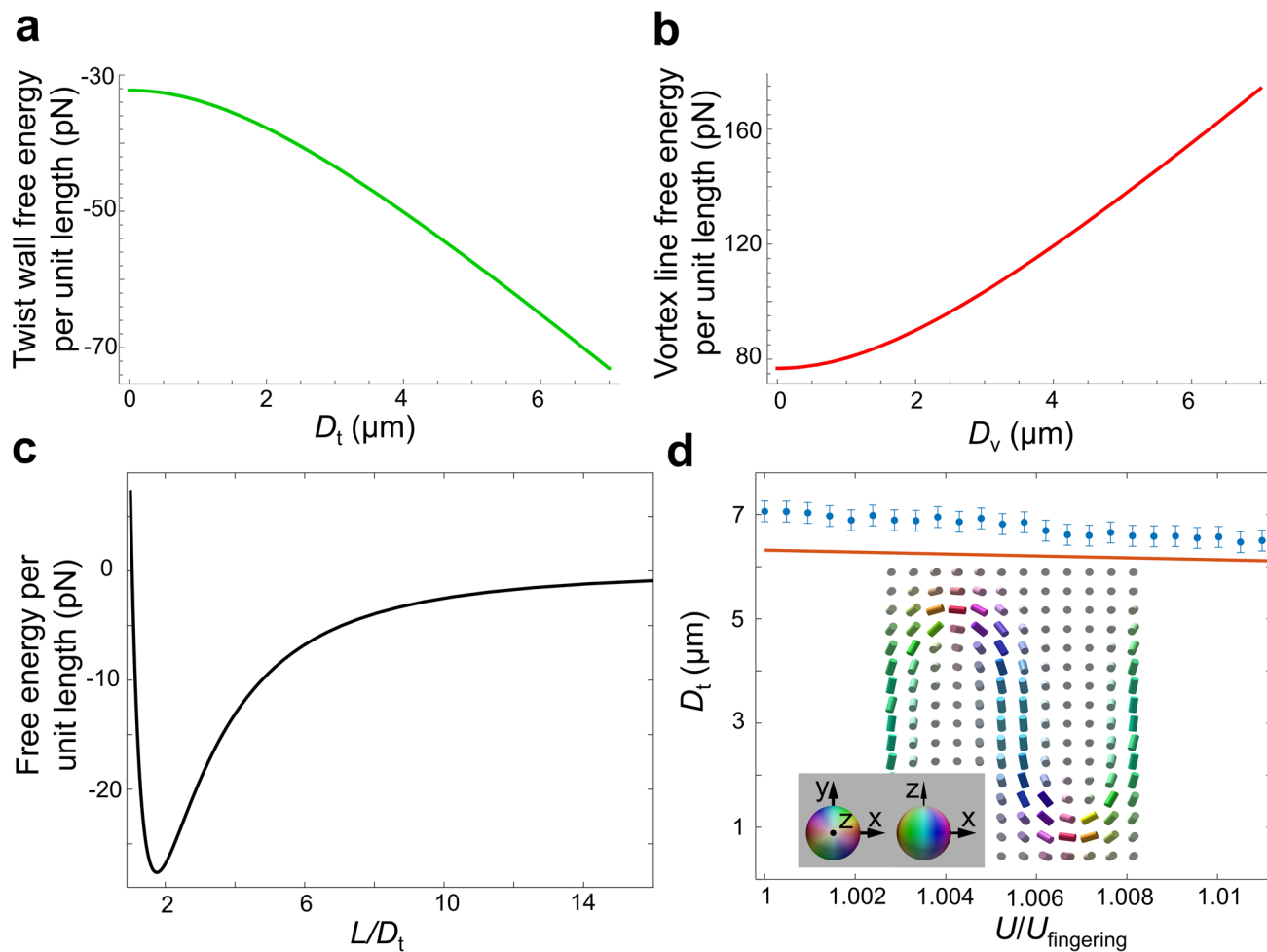
Extended Data Fig. 9 | Details of the energetic analysis of spontaneous folding. a, **b**, Free energy contributions per unit length of the möbiuson structure [Eq. (4)] from twist wall (**a**) and vortex line (**b**) versus respective displacement amplitudes; $D_v = D_t$ is assumed for the twist wall energy calculation. **c**, Free energy per unit length versus L/D_t with respect to a straight fibre-like structure. The energy was calculated using energy-minimizing D_v when varying L/D_t. A local minimum is found at $L/D_t \approx 1.75$, where experimental D_t values are used in the calculation. **d**, Theoretically predicted equilibrium twist wall displacement (red solid line) and experiment results (blue circle) under different values of voltage ($U_{fingering} = 2.970$V); experimental D_t values are measured with an error $\pm 0.2\mu$m, corresponding to the error bars. A computer-simulated cross-section in the horizontal midplane is shown in the inset.